

Study on Damage Evolution Mechanism of Rock-Soil Mass of Accumulation Slope Based on Shaking Table Test

Changwei Yang

Southwest Jiaotong University

Xinhao Tong

Southwest Jiaotong University

Zhifang Zhang

China National Railway Group Co., Ltd.

Sujian Ma

Southwest Jiaotong University

Liang Zhang

Southwest Jiaotong University

Jing Lian (✉ 781510224@qq.com)

Chongqing University <https://orcid.org/0000-0002-9077-4661>

Research Article

Keywords: Earthquake, Slope, Sichuan-Tibet Railway, Modal analysis, Vibration Characteristics

Posted Date: August 9th, 2021

DOI: <https://doi.org/10.21203/rs.3.rs-644142/v1>

License: © ⓘ This work is licensed under a Creative Commons Attribution 4.0 International License.

[Read Full License](#)

1 **Study on Damage Evolution Mechanism of Rock-Soil Mass of**
2 **Accumulation Slope Based on Shaking Table Test**

3 Authors' names:

4 Changwei Yang¹, Xinhao Tong¹, Zhifang Zhang², Sujian Ma¹, Liang Zhang¹, Jing Lian^{3*}

5 Adress¹: School of Civil Engineering, Southwest Jiaotong University, No.111, First Section
6 North of Second Ring Road, Chengdu, Sichuan 610031, People's Republic of China.

7 Adress²: Department of Science and Technology Management, China Railingway, No.10,
8 Fuxing Road, Yangfangdian Street, Haidian District, Beijing 100084, People's Republic of
9 China.

10 Adress³: School of Civil Engineering, Chongqing University, No.174, Shazheng Street,
11 Shapingba District, Chongqing 400030, People's Republic of China.

12 *Corresponding Author E-mail: 781510224@qq.com.

13 **Declaration of Competing Interests**

14 The authors acknowledge there are no conflicts of interest recorded.

15

16 **Abstract** To investigate the seismic dynamic characteristics of the accumulation slope, a
17 slope of the Zheduo Mountain tunnel along the Sichuan-Tibet Railway in China was selected
18 as the prototype, based on dimensional analysis and similarity principle, two groups of model
19 tests were carried out at 50° accumulation slope and 60° accumulation slope to obtain the
20 dynamic response influenced by different amplitude of seismic wave. A transfer function
21 analysis method suitable for shaking table test is proposed. Based on the data pretreatment
22 method of eliminating trend terms and digital filter, the frequency response function was
23 calculated by method of average periodic chart. And the variation of frequency response
24 function was analyzed by Pearson correlation coefficient. At last, the least square iteration
25 method was used for modal analysis. It is found that the transfer function changes obviously
26 when both the slopes are destroyed, the weak interlayer has a significant influence on seismic
27 wave transmission. The modal analysis results show that with the increase of the excitation
28 intensity, the natural frequency decreases and the damping ratio increases.

29 **Key Word** Earthquake, Slope, Sichuan-Tibet Railway, Modal analysis, Vibration
30 Characteristics

31 Introduction

32 The high hill-river valleys in the southwest mountainous area of China are characterized by
33 strenuous cutting, fractured rock mass, bad stability and even loose accumulation bodies are
34 widely distributed. Under the impact of the collision between the Indian plate and the Eurasian
35 plates, active fractures are densely distributed. There are frequent earthquakes and high
36 intensity (Kumar *et al.*, 2021), which are prone to induce large-scale landslides. When the slope

37 collapses, the sliding mass has strong kinetic energy and high speed movement (Shinoda *et al.*,
38 2017), which can quickly destroy the ground infrastructure (Singh *et al.*, 2016).

39 The characteristics of earthquake seismic response are one of the research hotspots in recent
40 years. At present, scholars mainly studied from theoretical analysis, numerical simulation,
41 model test, field observation and other means, which have made great achievements in the site
42 parameters and ground motion characteristics of slope. The existing theoretical analysis
43 methods for slope ground motion are mainly represented by limit analysis method
44 (Michalowski, 2009; Michalowski *et al.*, 2018), discontinuous deformation analysis
45 (Beyabanaki *et al.*, 2016; Yu *et al.*, 2019) and pseudo-static method, calculate the safety
46 factor of slope, critical state of rupture and influencing factors of homogeneous soil; and
47 numerical simulation method are represented by finite difference (Liu *et al.*, 2004), finite
48 element (Yin *et al.*, 2019), discrete element (Valentino *et al.*, 2008), etc. The result is superior
49 to the calculation of the dynamic state of the slope and the related influencing factors (Assimaki
50 *et al.*, 2005; Paolucci, 2002; Pagliaroli *et al.*, 2014). But both the theoretical method and the
51 numerical simulation method have some shortcomings on the heterogeneous slope. Such as the
52 boundary effect of heterogeneous slope is difficult to consider, and the convergence problem
53 of numerical analysis, Trombetti *et al* (2002) analyzed the theoretical calculation results of
54 structure vibration through the linear system, and confirmed the reliability of the shaking table
55 test technology. Based on the above reasons, this paper chooses the shaking table test as the
56 research method.

57 In the Wenchuan earthquake that occurred in China, a large number of slope landslide
58 damage occurred. As is shown in Fig.1, the slope angles of these slopes are different, resulting

59 in different forms of slope damage. As a typical type of slope with weak interlayer widely
60 distributed, the failure of the accumulation slope is often due to the low elastic modulus and
61 strength of the internal structure. [Fan *et al* \(2016\)](#) studied the shaking table of bedding and anti-
62 dip weak interlayer, in which the weak interlayer presented a low gradient with the horizontal
63 surface, and analyzed the acceleration and spectral response results.

64 Transfer function is one of the common methods used to analyze structural vibration signals,
65 and some scholars have applied this method in engineering seismic response ([Kojima *et al.*,
66 2015](#); [Komoda *et al.*, 2015](#); [Sheng *et al.*, 2012](#); [Cui *et al.*, 2012](#); [Fan *et al.*, 2017](#)). Abundant
67 achievements have been made in the researches, but it can be found that the research on transfer
68 function of slope is not sufficient, and the calculation method of the transfer function is
69 relatively simplified, also the relationship between multi-mode modes and the influence of
70 noise is often ignored.

71 Taking the actual slope along the Sichuan-Tibet Railway as a prototype, based on 1:10
72 similar ratio for model and the prototype, two groups of the different gradient model slope were
73 simulated earthquake by excitation signal. On the basis of signal processing, using the method
74 of average periodic chart (Welch method) to calculate the acceleration frequency response
75 function of the surface and inside of model slope. Using Pearson correlation coefficient to
76 analyze the changes of the frequency response function after the different gradient of slope
77 with the increase input of amplitude of earthquake ground motion. Using the least square
78 iteration method to do the modal analysis, identifying the ground motion response
79 characteristics of the slope. The research results are beneficial to the identification of seismic
80 failure process and seismic study of the accumulation slope, and it can be extended to the

81 analysis of ground motion of heterogeneous slope.

82 Overview of shaking table test

83 In this paper, a slope of the Zheduo Mountain tunnel along the Sichuan-Tibet Railway in
84 China is selected as the prototype, its slope is about 60 degrees, in order to compare, a group
85 of 50° slope was used for the control experiment.

86 Zheduo Mountain is located in Ganzi Prefecture, Sichuan Province. The altitude of the
87 highest mountain is 4962 meters above sea level, and the notch is 4298 meters above sea level.
88 The altitude difference between the Zheduo Mountain and Kangding City is 1,800 meters,
89 which is the first high mountain notch that needs to be passed on the Sichuan-Tibet Railway.
90 Therefore, it is known as the "First Pass of Kangba". The photo of Zheduo Mountain is shown
91 in Fig.2. In terms of terrain, the region boundary is roughly on the west side of the pass from
92 Lanniba, Yulongxi to Zheduo Mountain. It was divided into two parts: mountains and extreme
93 mountains to the east, and mountain plains and western plateau canyons to the west. The
94 mountains and extreme mountains on the eastern slope of the Daxue Mountain are high and
95 with deep Dadu River, broken surface, steep valley slope, and the relative elevation difference
96 of the valley is 1000m ~ 3000m. The western slope of the Daxue Mountain plateau, the
97 elevation is about 4500m, the valley cut is shallow, while the top surface is open and smooth
98 with lush water and grass. Zheduo Mountain is a vein of Daxue Mountain, which is an
99 important geographical boundary. The west of the plateau uplift with Yalong River and the east
100 of the alpine valley with Dadu River. The peak of the Zheduo Mountain is 4,962 meters above
101 sea level, and the pass is 4,298 meters above sea level, with an altitude drop of 1,800 meters

102 from Kangding City. Due to the strong cutting of Minjiang River and Dadu River, the
103 geographical landform of the Zheduo Mountain Line is characterized by large elevation
104 difference, dense ravines, crossing mountains, dense trees and warm and moist climate, with
105 typical characteristics of subtropical warm and humid valley.

106 This paper is based on a typical accumulation slope at the entrance of Zheduo Mountain
107 tunnel. According to the data recorded by China Earthquake Networks, since 2012, this area
108 has been affected by approximately 204 earthquakes of $2.0 \leq M_s \leq 8.0$ (see Fig.3), most of them
109 are small earthquakes. A large number of frequent small earthquakes will cause a large amount
110 of damage and damage to the inside of the slope, providing conditions for large-scale collapse
111 in the later period, and thus seriously affecting the construction safety of the Zheduo Mountain
112 Tunnel. Therefore, it is urgent to research the dynamic feature of the slope under earthquake to
113 provide technical support for slope disaster prevention and control along the Sichuan-Tibet
114 Railway.

115 **Similar system**

116 The model similarity system adopted in this paper is implemented by the similar three
117 theorems (Yuan, 1998). It is believed that the parametric relations of the implementation
118 phenomenon can be converted into a function of the similarity criterion under the condition
119 that the similarity phenomenon satisfies. It is the same as the function of the similarity
120 phenomenon, also called π -theorem (Curtis *et al.*, 1998), that is namely Equation (1) and
121 Equation (2):

$$122 \quad f(a_1, a_2, \dots, a_k, a_{k+1}, a_{k+2}, \dots, a_n)=0 \quad (1)$$

$$123 \quad F(\pi_1, \pi_2, \dots, \pi_{n-k})=0 \quad (2)$$

124 In equation (1), a_1, a_2, \dots, a_k are the elementary quantity, and $a_{k+1}, a_{k+2}, \dots, a_n$ are the
125 derived quantity. In equation (2), $\pi_1, \pi_2, \dots, \pi_{n-k}$ Dimensionless constant. The matrix
126 method can be used to derive the similarity criterion of the physical model, is shown in Table
127 1. Among them, Geometric scale is L ; gravitational acceleration is g ; cohesion is c ; dynamic
128 elastic modulus is E ; internal friction angle is φ ; dynamic Poisson's ratio is μ ; gravity is γ ; shear
129 wave velocity is v_s ; input acceleration is A ; duration is T_d ; frequency is ω ; angular displacement
130 is θ ; linear displacement is s ; response speed is V ; response acceleration is a ; stress is σ ; strain
131 is ε .

132 In the case that phenomena and similar phenomena can be expressed as same functions.
133 Those which can be regarded as similar if they have similar individual parameters and equal
134 similarity criteria. According to the above criteria, the similarity relationship of the main
135 physical quantities in the model adopted in this paper, as is shown in Table 2.

136 **Test device and model**

137 This experiment adopted large one-way seismic simulation shaking table to simulate, the
138 model box floor and skeleton material is mainly composed of steel plate, gradient steel, iron
139 channel, to facilitate the observation and record in the test process of the model of slope
140 deformation and failure phenomena, and the model box is visualized with 12mm optical
141 plastics on both sides. Apply vaseline evenly between optical plastics and model to reduce
142 friction. Using a 10 cm thick foamed polyethylene to reduce boundary effect between model
143 and boundary. The bottom board of the model box is adhesive stone columns with epoxy resin
144 to make it a rough surface to reduce the relative displacement between the model box and the
145 model contact surface.

146 To satisfy the needs of the experiment, taking the slope relying on engineering drilling data
147 as the background, this paper adopted two kinds of gradients natural slope model, 50° and 60°
148 respectively. And the model of total 1.5 m high, 1.2 m high of side slope. To adapt the
149 characteristics of side slope, the side slope model is 2.21 m at the bottom, the vertical section
150 of the model is consistent with a width of 2m, the bedrock is 0.25m high. The weak interlayer
151 is covered on the bedrock with a thickness of 5 cm, and the accumulation mass is covered on
152 the weak interlayer. The basic physical parameters of the test model material can be obtained
153 through laboratory tests, as is shown in Table 3.

154 The test model was made on site. In the process of filling the model, it was filled layer by
155 layer and bottom-up, with one density test for each fill of 20 cm. And compaction was carried
156 out by artificial vibration, that is, the central part and boundary of the model were compacted
157 by artificial compaction to ensure the compaction quality, as shown in Fig.4. The overall model
158 is shown in Fig.5, the gradient is the angle between the overlying accumulation body and the
159 level surface. The layout of the measuring point adopted in this paper is shown in Fig.6, as it
160 shows, it mainly divided into two categories, the acceleration sensor distribution in free field,
161 central slope surface, the interface between bedrock and weak interlayer, the interface from
162 weak interlayer to accumulation body as well as the free field. And displacement sensors are
163 mainly distributed at the top, middle and bottom slope surface, sensor sampling frequency is
164 1000 Hz.

165 **Loading cases and measuring points layout**

166 The white noise and seismic wave were simulated by inputting acceleration time histories in
167 shaking table, and the loading direction was horizontal along the slope surface. In this paper,

168 the input for the two groups of shaking table tests includes the following working conditions,
169 as shown in Table 4. In the table, white noise comes from measured data, as shown as Fig.7,
170 the first loading of white noise was mainly to reduce the random disturber and transient effect.
171 After loading was to scan the slope as a whole by loading white noise while reducing the
172 transient effect, so as to analyze the structural characteristics by using the transfer function
173 method, the seismic wave contains: Wenchuan wave, Kobe wave and EL Centro wave. The
174 amplitude normalization of the earthquake waveform loaded in this paper is shown in Fig.8~10.

175 **Slope failure phenomenon**

176 In the seismic wave loading process of the two groups of shaking table tests, the HD camera
177 system was used to shoot the phenomenon. The test results showed that the 50° slope had
178 obvious failure when the input Wenchuan wave peak acceleration was 0.6g, while the 60° slope
179 had the relatively similar phenomenon when it was 0.5g. The test phenomenon was shown in
180 Fig.11~12. The two groups of slope failure phenomena are similar, in which the debris flow
181 occurred in the deposited mass when the slopes were destroyed. At the same time, the slope
182 surface was partially deformed. The slope was greatly deformed and a large amount of debris
183 flow was generated when the 60° slope is destroyed. The slope surface was deformed a lot,
184 generating a lot of debris flow. Obvious back edge expansion crack appeared at the top of the
185 accumulation mass of the two groups of slopes. According to the monitoring data of
186 displacement sensors, as Fig.13 shows, the top displacement of the 60° slope is larger, and the
187 bottom displacement of the 50° slope is larger, but its displacement change trend is similar. It
188 means that slope failure mainly occurs along the weak interlayer plane in the overall collapse.
189 In addition, the displacement monitoring data of the slopes shows that the slopes of the two

190 slopes have a "step-off" change curve, which is consistent with the two energy fluctuations in
191 the Wenchuan earthquake waveform. According to the video and sensor monitoring data, the
192 failure stages of the slope under both working conditions are as follows: first, the slope surface
193 appeared cracks and deforms, the accumulation body squeezed the weak interlayer and
194 develops downward, and cracks may appear between the accumulation mass and the weak
195 interlayer. Subsequently, the movement of superstructure (accumulation mass) and
196 substructure (weak interlayer and bedrock) were gradually inconsistent during the earthquake.
197 Finally, the movement of the superstructure was greater than that of the substructure, and tensile
198 cracks appeared at the back edge of the accumulation body (Moore *et al.*, 2011), at the same
199 time, the cracks in the interface gradually developed and broke through the locked section, and
200 finally the overall failure occurred, as Fig.14 shows.

201 Calculation method of seismic transfer function of slope

202 Transfer function is the main methods to study control theory, which embodies the
203 transformation relationship between input signal and output signal, and theoretically is
204 irrelevant with input parameters. In structural dynamics, the transfer function can describe the
205 motion law of the structure and analyze the dynamic characteristics and stability of the system.

206 **Structural seismic frequency response function**

207 In a single-degree-of-freedom linear structure, its non-time-dependent vibration motion
208 equation is written as Equation (3):

$$209 \quad ax(t) + b\dot{x}(t) + c\ddot{x}(t) = f(t) \quad (3)$$

210 Among them, $x(t)$ 、 $\dot{x}(t)$ and $\ddot{x}(t)$ are the displacement, speed and acceleration time

211 histories of the point particle respectively. And a 、 b and c are all constants and determined
212 by the initial state of the object. The Laplace-transformation of Equation (3) is Equation (4):

$$213 \quad (s^2 + 2\xi\omega_0s + \omega_0^2)X(s) = \frac{F(s)}{c} \quad (4)$$

214 Where, s is a complex variable, above equations are equivalent to the Fourier transform
215 when $Re(s) = 0$, and ω_0 is the inherent circular frequency of the structure.

216 Let $X(s)$ and $F(s)$ be the displacement and displacement exerted on the structure
217 respectively, then the Laplace-transforms of the two are Equations (5) and (6) respectively:

$$218 \quad X(s) = \int_0^{+\infty} x(t)e^{-st}dt \quad (5)$$

$$219 \quad F(s) = \int_0^{+\infty} f(t)e^{-st}dt \quad (6)$$

220 After dividing the above equations, the displacement transfer function of the structure can
221 be obtained as Equation (7):

$$222 \quad H_d(s) = \frac{1}{c(s^2 + 2\xi\omega_0s + \omega_0^2)} \quad (7)$$

223 In the above Equation (7), ξ is the damping ratio. Similarly, velocity transfer function
224 Equation (8) and acceleration transfer function Equation (9) can be obtained:

$$225 \quad H_v(s) = \frac{s}{c(s^2 + 2\xi\omega_0s + \omega_0^2)} \quad (8)$$

$$226 \quad H_a(s) = \frac{s^2}{c(s^2 + 2\xi\omega_0s + \omega_0^2)} \quad (9)$$

227 From the above formula, the transfer function is a complex-valued function, which is
228 represented as a curved surface in the Laplace Domain. Therefore, frequency response analysis
229 and root locus method are often used to describe the transfer function in practical applications,
230 among which the former is the main approach. Due to space limitation, taking the displacement
231 frequency response function as an example, Equation (7) can be written in the frequency
232 domain as Equation (10):

233
$$H_d(\omega) = \frac{j\omega}{c(\omega_0^2 - \omega^2 + 2j\xi\omega_0\omega)} \quad (10)$$

234 Considering that the initial state of the structure is stationary under the action of earthquake,
 235 the real part is 0, and the imaginary part is angular frequency. The frequency domain response
 236 of the structure under the action of earthquake is shown in Equation (11):

237
$$X(\omega) = \int_{-\infty}^{+\infty} x(t)e^{-i\omega t} dt \quad (11)$$

238 Where, ω is the angular frequency variable, $X(\omega)$ is the complex function of ω , $x(t)$ is
 239 the vibration signal, i is the imaginary number. Taking frequency as independent variable, the
 240 real part of can be expressed as the real frequency curve of the signal, and the imaginary part
 241 of can be expressed as the virtual frequency curve of the signal. $X(\omega)$ can be expressed in the
 242 module and vector form as Equation (12):

243
$$X(\omega) = |X(\omega)|e^{-i\theta(\omega)} \quad (12)$$

244 Taking frequency as an independent variable, $|X(\omega)|$ can be expressed as the amplitude-
 245 frequency curve of the signal, and $\theta(\omega)$ as the phase-frequency curve of the signal.

246 Substituting Equation (10) into Equation (12), its amplitude versus frequency and phase
 247 frequency are Equation (13) and Equation (14) respectively:

248
$$|H_d(\omega)| = \frac{1}{c\sqrt{(\omega_0^2 - \omega^2)^2 + (2\xi\omega_0\omega)^2}} \quad (13)$$

249
$$\varphi(\omega) = \arctan \frac{-2\xi\omega_0\omega}{\omega_0^2 - \omega^2} \quad (14)$$

250 Take $|H_d(\omega)|$ to ω to calculate the extreme value. Since ξ is small, it is generally
 251 considered as 0.05 in engineering. Then, the frequency corresponding to the peak amplitude
 252 versus frequency is shown in Equation (15):

253
$$\omega_0' = \omega = \omega_0\sqrt{1 - 2\xi^2} \approx \omega_0 \quad (15)$$

254 At this point, ω_0 is believed to be the natural circular frequency, and modal analysis can be

255 performed accordingly. If a , b and c in Equation (3) are replaced by system mass matrix
256 $[M]$, damping matrix $[C]$, and stiffness matrix $[K]$, modal identification can be carried out
257 accordingly.

258 According to the above theory, the transfer function method represents the ratio of input and
259 output. And the frequency response function method is a subset of the transfer function method
260 and is the ratio of response to incentive. Therefore, it is suitable for the analysis of nonlinear
261 random vibration signals represented by earthquakes.

262 **Data pre-processing**

263 In the shaking table test, due to the existence of various kinds of interference, it is often
264 necessary to pre-process the vibration signal to make the sampling frequency as close to the
265 true value as possible. In this paper, the eliminating trend term and digital filter are used to pre-
266 process the collected data.

267 The polynomial least-squares is commonly used to eliminate the trend term, and the order
268 of eliminating trend term adopted in this paper is order 5.

269 In the model test, as the collected disperse cosine signals contain a variety of sources, digital
270 filter is needed to filter out the noise or false components in the test signals. In this paper, taking
271 FIR filters and implemented through the window method. In order to pay attention to the
272 different contributions of each frequency component in different frequency bands, taking the
273 Hanning window can widen the major lobe and the side lobe can offset each other to the
274 maximum extent to get more effective suppression of leakage. Therefore, the Hanning window
275 is selected in this paper, and its calculation formula is Equation (16):

276
$$\omega(t) = \begin{cases} \frac{1+\cos\frac{\pi t}{T}}{2} & (0 \leq t \leq T) \\ 0 & (t > T) \end{cases} \quad (16)$$

277 **Frequency response function calculation**

278 The transfer function calculation for random vibration signals is usually realized by the
 279 power spectral density function (Jin *et al.*, 2020), which is the Fourier transform of the signal
 280 auto-correlation function. In this paper, the average periodic diagrams (Welch method) is used
 281 to calculate it. The frequency response function is calculated as the quotient obtained by
 282 dividing the cross-power spectral density function $S_{xy}(k)$ of the excitation signal and the
 283 corresponding signal by the self-rate spectral density function $S_{xx}(k)$ of the excitation signal,
 284 that is Equation (17) :

285
$$H(k) = \frac{S_{xy}(k)}{S_{xx}(k)} \quad (17)$$

286 Where, $S_{xy}(k)$ and $S_{xx}(k)$ are defined as Equations (18) and (19) respectively:

287
$$S_{xy}(k) = \frac{1}{MN_{FFT}} \sum_{i=1}^M X_i(k) Y_i^*(k) \quad (18)$$

288
$$S_{xx}(k) = \frac{1}{MN_{FFT}} \sum_{i=1}^M X_i(k) X_i^*(k) \quad (19)$$

289 In the above formula, $X_i(k)$ and $Y_i(k)$ are the Fourier transform of the i th data segment
 290 of one or two random vibration signals. $X_i^*(k)$ and $Y_i^*(k)$ are the conjugate complex
 291 numbers of $X_i(k)$ and $Y_i(k)$ respectively. And M is the average degree.

292 In this paper, the sampling frequency was taken as 1000Hz, the fast Fourier transformation
 293 (FFT) length was set as 2048. The excitation signal was the acceleration signal collected by the
 294 measuring point A0, and the results were analyzed according to the distribution of measuring
 295 points at different positions. It can be seen from Equations (11) that the frequency response
 296 function can be represented by real frequency and imaginary frequency or amplitude versus

297 frequency and phase. The former is more often used in use. The data frequency collected in
298 this paper is 1000Hz, and high-frequency sampling leads to a wide frequency range of random
299 interfering signals, which accounts for a large proportion. Therefore, there are many glitches
300 after the collected data are plotted, which are not smooth, data smoothing can eliminate burrs
301 and the influence of higher-order trend terms can also be eliminated. The data smoothing
302 method selected in this paper is the five-spot triple smoothing method, because it can smooth
303 the signal in both time domain and frequency domain, effectively reduce the high-frequency
304 random noise. When analyzing the frequency response function, the intersection of the real
305 frequency characteristic curve and the frequency axis of the multi-degree of freedom system is
306 prone to horizontal movement. Under the influence of near modes, the imaginary frequency is
307 usually used for analysis. Pearson correlation coefficient can be used to analyze the variation
308 of frequency response function, currently, the commonly used judgment criteria in the
309 engineering field were shown in Table 5.

310 Seismic response analysis of slope based on transfer function

311 Slope surface measuring point

312 The acceleration of the measuring point A0 was taken as the excitation signal. The point A1
313 in the middle of the slope surface was selected as the response signal to calculate the frequency
314 response function after the input of seismic waves of different excitation intensity. The results
315 were shown in Fig.15 and Fig.16. It can be clearly observed from Fig.15 that, when the 50°
316 slope is loaded, the real frequency and imaginary frequency parts of the frequency response
317 function of A1 measuring point are relatively similar before the excitation intensity is 0.5g.

318 While the real frequency and imaginary frequency parts of the loaded seismic wave change
319 obviously after the excitation intensity is 0.5g, both the real frequency and the imaginary
320 frequency parts of the first-order natural frequency become smaller. The increase of the
321 amplitude of the signal fluctuation indicates that the structure appears damage deformation in
322 the signal transmission from measure point A0 to measure point A1. The Fig.16 shows that as
323 the excitation intensity increases, frequency response function of the measured points A1 of 60°
324 slope has changed, real frequency and the imaginary frequency part of the first order natural
325 frequency and the corresponding amplitudes were gradually reduced. Before the excitation
326 intensity was 0.4g, the variation rules of the real frequency and the imaginary frequency parts
327 were similar of 60° slope, and the frequency response function changed significantly when the
328 excitation intensity was 0.4g and 0.5g.

329 Taking the frequency response function of the point A1 on the slope surface when the
330 excitation intensity is 0.1g as the reference. With the excitation intensity increases, the variation
331 law of the correlation coefficient of the frequency response function shown in Fig.17.
332 According to the definition of correlation coefficient, both the real frequency and the imaginary
333 frequency of a 50° slope are greater than 0.8 before the excitation intensity is 0.6g, which
334 indicates a high correlation. Thereafter, the correlation coefficient decreased significantly and
335 was less than 0.8. Similarly, the real frequency and imaginary frequency parts of 60° slope are
336 highly correlated before the excitation intensity is 0.4g, when the excitation intensity is 0.4g,
337 the correlation coefficient of 60° slope will be severely reduced, however, the slope surface
338 will not be damaged until the excitation intensity is 0.5g. This indicates that cracks may have
339 appeared in the structure when the excitation intensity is 0.4g. By comparison, it can be seen

340 that the frequency response function of the 60° slope decreases more sharply than that of the
341 50° slope, which is consistency with the failure phenomenon of the slope.

342 **Effects of the weak interlayer**

343 Similarly, the frequency response functions of the accelerations at points A2 to A5 on both
344 sides of the weak interlayer of the slope were calculated based on the accelerations at points
345 A0. The correlation coefficient of the frequency response function of the above measurement
346 points for 50°slope and 60°slope can be calculated based on the excitation intensity is 0.1g, as
347 shown in Fig.18 and Fig.19. In Fig.18, the real frequency part of each measuring point is
348 relatively similar. In the case of slope failure, the imaginary frequency correlation coefficient
349 of both the point A2 and the point A4 are < 0.8 . The real frequency correlation coefficient of
350 the A4 measuring point is the smallest. In terms of the correlation coefficient of the imaginary
351 frequency part, each measurement point is obviously different, which is shown as $A2 < A3, A4$
352 $< A5$, and $A2 < A4$. The phenomenon shows that the signal changes significantly after the
353 seismic wave passes through the weak interlayer, leading to the occurrence of motion
354 inconsistency. The failure of the slope is due to the penetration of the fracture from the point
355 A2 to the point A4, rather than the development of the fracture at the back edge of the top of
356 the slope. Fig.19 shows that the variation trend of the correlation of the frequency response
357 function of the 60° slope is similar to that of the 50° slope. The real frequency part changes
358 little and the law is not obvious, so it should be affected by the near modes. The change of
359 imaginary frequency is more obvious, in which the correlation coefficient of point A2 point is
360 less than that of point A4. It indicates that the crack in the slope body evolves from the lower
361 part to the upper part and is still a traction landslide, which is inconsistent with the surface

362 displacement of the slope and may be due to the movement form of the accumulation body.
363 The correlation coefficient of point A3 is lower than that of point point A2, which may be due
364 to the large own weight of the deposited mass at point A2, structure center is at the front, the
365 seismic wave transmission first arrives at point A2 and then arrives at point A3. In addition, the
366 correlation coefficient is less than 0.4 when the excitation intensity is 0.5g, it should be caused
367 by the signal fluctuation after the structure is damaged and cracks appear.

368 It can be seen from the above phenomena that the sliding of the experimental slope is mainly
369 due to the occurrence of cracks between the accumulation mass and the weak interlayer caused
370 by the earthquake. The obvious movement of the bedrock and the accumulation mass is
371 inconsistent. Under the horizontal force of the earthquake and the gravity along the weak
372 interlayer zone, the cracks between the soil are constantly expanding, the of the “anchor section”
373 shear surface is broken, the cracks gradually develop and extend, and finally the penetration
374 cracks appear, and the slope collapses. It can be expressed as shear-slide-fall type, which
375 belongs to traction landslide.

376 Modal analysis

377 The frequency response function can also be used for modal analysis of vibration signals.
378 The white noise input in this test can be regarded as the environmental excitation, therefore,
379 white noise can be used to identify the modal parameters of the vibration signal. The lowed
380 recognition accuracy can be avoided by avoiding the signal side-lope and low resolution in the
381 ground motion response signal, currently, the methods commonly used in modal analysis
382 include the half-power bandwidth method, the admittance circle method, etc, the former is

383 based on the single-degree-of-freedom structure, the latter only uses the least square rationale
384 to estimate the radius or mode shape of conductance circle (Nyquist plot). The least-square
385 iteration method is a classical solution method based on analytic expressions to numerically fit
386 the real frequency response function data, it can obtain the best fitting between the test data
387 and the mathematical model in the sense of the least square. The calculation formula is shown
388 in Equation (20).

$$389 \quad H_{pq}(\omega) = -\sum_{i=1}^N \left(\frac{A_{ipq}}{j\omega - s_i} + \frac{A_{ipq}^*}{j\omega - s_i^*} \right) \omega^2 \quad (20)$$

390 Among them, N is the free degree of structure, s_i and A_{ipq} are polar points and remained
391 number of the i-th mode of frequency response function, and s_i^* and A_{ipq}^* are the conjugate
392 complex numbers of the first two. By substituting equation (23) into equation (8) and setting
393 the initial damping factor as 0.05, the vibration coefficient, eigen frequency ω_i and damping
394 ratio ξ_i of each mode can be calculated. In this paper, A1 is taken as the target to represent the
395 overall mode of the slope, the frequency of the first 3 order frequency response function is
396 taken for identification. As shown in Fig.20, according to the fitting curve of the test condition
397 under the failure state, the calculated results are close to the measured results.

398 Fig.21 shows the vibration coefficients of the first three modes obtained by calculation. It
399 can be seen from the Fig.21 that the vector of the first vibration mode of the two groups of
400 slopes is significantly larger than that of the second and the third. This indicates that the slope
401 vibration is mainly controlled by the first mode of vibration. However, the magnitude of the
402 second mode vector of the in some cases under excitation intensity is large, and it means that
403 the seismic mode of the slope under this gradient is relatively complex and can be regarded as
404 having two degrees of freedom. Represented by two groups of measuring points on the slope

405 surface, the natural frequency and damping ratio of the first mode (main mode) of the slope in
406 the measured group were calculated and observed. It is worth mentioning that, empirically,
407 some scholars believe that it is spurious mode when the damping ratio $>20\%$. However, due to
408 the large discreteness of soil and the wide frequency band of white noise, the calculated
409 damping ratio will be larger, therefore, this paper believes that the calculated results are reliable
410 in trend. It can be seen from Fig.22 that, with the increase of the excitation intensity, the natural
411 frequency of the slope was decreases in trend. Assume that the weight of the test model will
412 not change when the damping ratio is not taken into account, the reduction of the natural
413 frequency indicates that the lateral stiffness of the structure decreases. The increase in the
414 damping ratio indicates that cracks and expansion occurred in the test model, resulting in
415 increase of friction between soils and enhanced energy absorbing action, therefore, the damping
416 ratio increases. Meanwhile, under the same intensity seismic wave, the comparison shows that
417 the damping ratio of a 60° slope is higher than that of a 50° slope, the 60° slope natural
418 frequency is less than that of the 50° slope, indicating that the higher the gradient is, the less the
419 anti-lateral stiffness will be, while the internal friction of soil mass will be more obvious.

420 Conclusions

421 This paper is based on a typical accumulation slope at the entrance of Zheduo Mountain
422 tunnel, shaking table model tests of the 50° accumulation slope and 60° accumulation slope
423 respectively were carried out. The displacement and acceleration of the slope were tested, the
424 dynamic characteristics of the measuring point were analyzed using the transfer function, and
425 the modal analysis was carried out. The main conclusions are as follows:

426 (1) Under the action of earthquake, the failure of the overlying slope is mainly the overall
427 collapse along the weak interlayer zone, the slope displacement of the slope is relatively
428 consistent. At the same time, debris flow was generated on the slope surface. The 50° slope
429 was destroyed when the peak acceleration of Wenchuan earthquake wave was 0.6g, the 60°
430 slope was destroyed when the peak acceleration of Wenchuan earthquake wave was 0.5g. At
431 the top of the accumulation mass, there were obvious expanding cracks at the back edge.

432 (2) Based on the data pre-processing and average periodic diagrams method, the transfer
433 function can be calculated and reflecting the vibration characteristics of the accumulation slope.
434 Pearson correlation coefficient and modal analysis can be used to analyze the structural
435 characteristics reflected by the transfer function. The analysis method can be well applied to
436 the slope shaking table test.

437 (3) The frequency response function of accumulation slope can be analyzed from two aspects:
438 slope surface and slope interior. Based on the frequency response function by white noise
439 scanned after the excitation intensity is 0.1g, on the slope surface, the correlation coefficient
440 50° slope significantly decreased and was destroyed after the excitation intensity is 0.6g, while
441 the correlation coefficient of 60°slope significantly decreased after the excitation intensity is
442 0.4g, failure will not occur until the excitation intensity is 0.5g. With the increase of the
443 excitation intensity, the correlation coefficient of the 60°slope is lower than that of 50° slope
444 and drop more. The correlation coefficient of the slope failure are all < 0.8 . Inside the slope,
445 the correlation coefficient of frequency response function at the point A2 decreased less than
446 that at the point A4, it means that the crack in the slope developed from the lower part to the
447 upper part, the correlation coefficients between point A2 and point A3, point A3 and point A4

448 were significantly different, and it shows that the weak interlayer had a significant influence
449 on seismic wave transmission. Based on the slope displacement and frequency response
450 function, it can be seen that the slope in this test is retrogressive failure under the action of
451 earthquake.

452 (4) Using the least-square iteration method to analyze the frequency response function can
453 be used for the modal identification and analysis of accumulation slope. Represented by the
454 point on the slope surface, the two groups of slopes are mainly affected by the first mode and
455 second mode of vibration. With the increase of the excitation intensity, the post-earthquake
456 damping ratio of 50°slope increased more on the 60°slope, and the natural frequency of
457 60°slope decreased more on 50°slope.

458 Data and Resources

459 The data used to support the findings of this study are available from the corresponding author upon request.

460 Acknowledgments

461 This research was financially supported by National Natural Science Foundation of China (No.52078426);
462 National Key Research and Development Plan (NO.2018YFE0207100); Sichuan Provincial Science and
463 Technology Support Project (NO.2020YJ0253, c).

464 References

465 Assimaki, D., E. Kausel, and G. Gazetas (2005). Wave propagation and soil-structure interaction on a cliff crest
466 during the 1999 Athens Earthquake, *Soil Dyn. Earthq. Eng.* **25** 513-527.

467 Beyabanaki, S. A. R., A. C. Bagtzoglou, and L. B. Liu (2016). Applying disk-based discontinuous deformation

468 analysis (DDA) to simulate Donghekou landslide triggered by the Wenchuan earthquake, *Geomech. Geoenviron.*
469 **11** 177-188.

470 Cui, Z., Q. Sheng, Y. Song, and Q. Wei (2012). Application of transfer function to stochastic seismic response
471 analysis of underground caverns, *Rock and Soil Mechanics* **33** 3760-3766.

472 Curtis, W. D., J. D. Logan, and W. A. Parker (1982). Dimensional analysis and the pi theorem, *Linear Algebra*
473 *and its Applications* **47** 117-126.

474 Fan, G., J.-j. Zhang, and X. Fu (2017). Research on transfer function of bedding rock slope with soft interlayers
475 and its application, *Rock and Soil Mechanics* **38** 1052-1059.

476 Fan, G., J.-j. Zhang, X. Fu, and L.-r. Zhou (2016). Dynamic failure mode and energy-based identification
477 method for a counter-bedding rock slope with weak intercalated layers, *Journal of Mountain Science* **13** 2111-
478 2123.

479 Jin, Z., Q. Han, K. Zhang, and Y. Zhang (2020). An intelligent fault diagnosis method of rolling bearings based
480 on Welch power spectrum transformation with radial basis function neural network, *Journal of Vibration and*
481 *Control* **26** 629-642.

482 Kojima, K., K. Sakaguchi, and I. Takewaki (2015). Mechanism and bounding of earthquake energy input to
483 building structure on surface ground subjected to engineering bedrock motion, *Soil Dyn. Earthq. Eng.* **70** 93-103.

484 Komoda, K., M. Sakuma, M. Yata, Y. Yamazaki, F. Imaizumi, R. Kuroda, and S. Sugawa (2015). Measurement
485 and Analysis of Seismic Response in Semiconductor Manufacturing Equipment, *Ieee Transactions on*
486 *Semiconductor Manufacturing* **28** 289-296.

487 Kumar, V., I. Jamir, V. Gupta, and R. K. Bhasin (2021). Inferring potential landslide damming using slope
488 stability, geomorphic constraints, and run-out analysis: a case study from the NW Himalaya, *Earth Surface*
489 *Dynamics* **9** 351-377.

490 Liu, C., S. Qi, L. Tong, and F. Zhao (2004). STABILITY ANALYSIS OF SLOPE UNDER EARTHQUAKE
491 WITH FLAC3D, Chinese Journal of Rock Mechanics and Engineering **23** 2730-2733.

492 Michalowski, R. L. (2009). Expanding collapse in partially submerged granular soil slopes, Canadian
493 Geotechnical Journal **46** 1371-1378.

494 Michalowski, R. L., A. Wojtasik, A. Duda, A. Florkiewicz, and D. Park (2018). Failure and Remedy of Column-
495 Supported Embankment: Case Study, Journal of Geotechnical and Geoenvironmental Engineering **144**.

496 Moore, J. R., V. Gischig, J. Burjanek, S. Loew, and D. Faeh (2011). Site Effects in Unstable Rock Slopes:
497 Dynamic Behavior of the Randa Instability (Switzerland), Bulletin of the Seismological Society of America **101**
498 3110-3116.

499 Pagliaroli, A., B. Quadrio, G. Lanzo, and T. Sano (2014). Numerical modelling of site effects in the Palatine
500 Hill, Roman Forum, and Coliseum Archaeological Area, Bulletin of Earthquake Engineering **12** 1383-1403.

501 Paolucci, R. (2002). Amplification of earthquake ground motion by steep topographic irregularities, Earthquake
502 Engineering & Structural Dynamics **31** 1831-1853.

503 Sheng, Q., Z. Cui, J. Liu, and X. Leng (2012). Application study of transfer function for seismic response
504 analysis of underground engineering, Rock and Soil Mechanics **33** 2253-2258.

505 Shinoda, M., and Y. Miyata (2017). Regional landslide susceptibility following the Mid NIIGATA prefecture
506 earthquake in 2004 with NEWMARK'S sliding block analysis, Landslides **14** 1887-1899.

507 Singh, H., and S. K. Som (2016). Earthquake triggered landslide-Indian scenario, Journal of the Geological
508 Society of India **87** 105-111.

509 Trombetti, T. L., and J. P. Conte (2002). Shaking table dynamics: Results from a test-analysis comparison study,
510 Journal of Earthquake Engineering **6** 513-551.

511 Valentino, R., G. Barla, and L. Montrasio (2008). Experimental analysis and micromechanical modelling of dry

512 granular flow and impacts in laboratory flume tests, *Rock Mechanics and Rock Engineering* **41** 153-177.

513 Yin, C., W.-h. Li, C.-g. Zhao, and X.-a. Kong (2019). Impact of tensile strength and incident angles on a soil
514 slope under earthquake SV-waves, *Engineering Geology* **260**.

515 Yu, P., Y. Zhang, X. Peng, J. Wang, G. Chen, and J. X. Zhao (2019). Evaluation of impact force of rock
516 landslides acting on structures using discontinuous deformation analysis, *Computers and Geotechnics* **114**.

517 Yuan, W. Z. (1998). Similarity theory and statics model test, Southwest Jiaotong University Press, Sichuan.

518 **Full mailing address for each author**

519 Changwei Yang, Jiulidi Campus, Southwest Jiaotong University, No. 111, North 1st Section of Second Ring Road,
520 Jinniu District, Chengdu City, Sichuan Province, PRC, 610031.

521 Xinhao Tong, Jiulidi Campus, Southwest Jiaotong University, No. 111, North 1st Section of Second Ring Road,
522 Jinniu District, Chengdu City, Sichuan Province, PRC, 610031.

523 Zhifang Zhang, No.10 Fuxing Road, Yangfangdian Street, Haidian District, Beijing City, PRC, 100844.

524 Sujian Ma, Jiulidi Campus, Southwest Jiaotong University, No. 111, North 1st Section of Second Ring Road,
525 Jinniu District, Chengdu City, Sichuan Province, PRC, 610031.

526 Liang Zhang, Jiulidi Campus, Southwest Jiaotong University, No. 111, North 1st Section of Second Ring Road,
527 Jinniu District, Chengdu City, Sichuan Province, PRC, 610031.

528 Jing Lian, No. 174, Shapingba Main Street, Shapingba District, Chongqing City, PRC, 400044.



529

530

(a) Wangjiayan Landslide



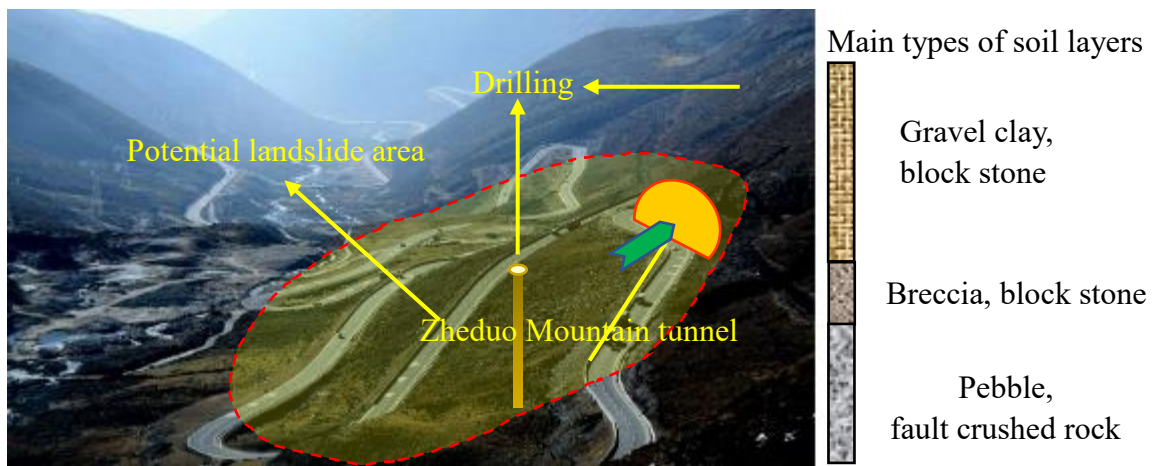
531

532

(b) The Baocheng Railway 109 tunnel collapsed

533

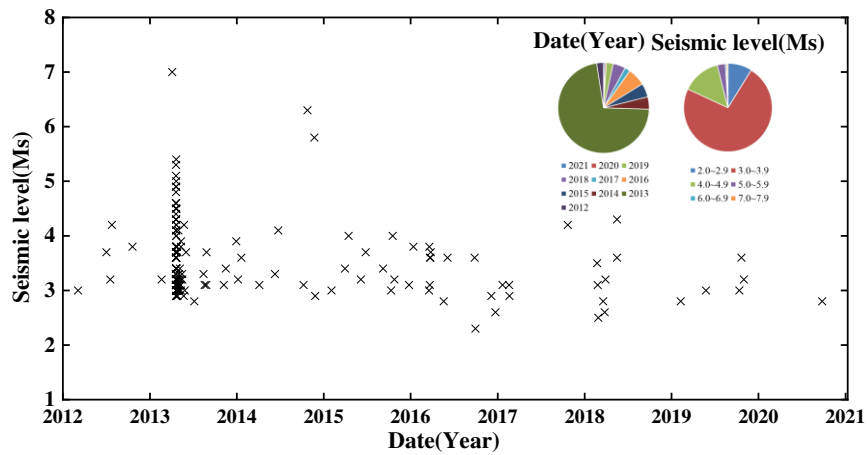
Fig.1 Site of landslide caused by Wenchuan earthquake



534

535

Fig.2 The landform of the Zheduo Mountain



536

537

Fig.3 Historical seismogenic situation near the slope supporting project



538

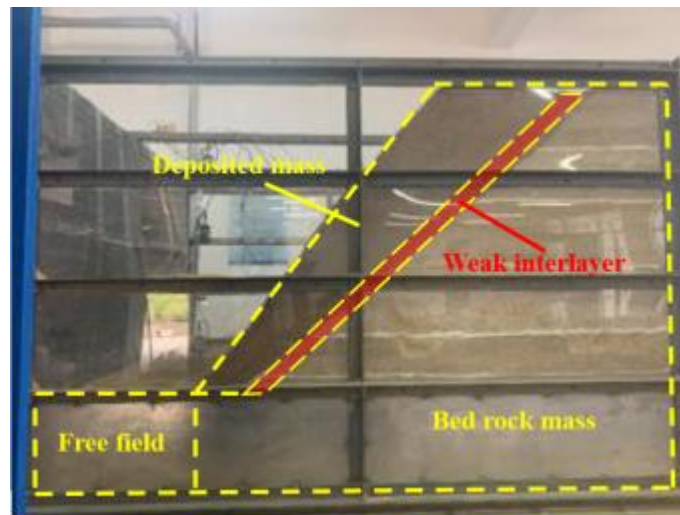
539

(a) Model filling

(b) Physical parameter test

540

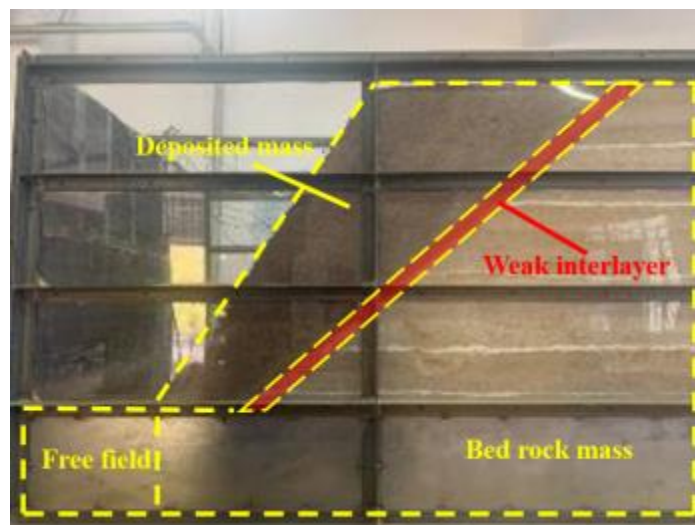
Fig.4 Model preparation



541

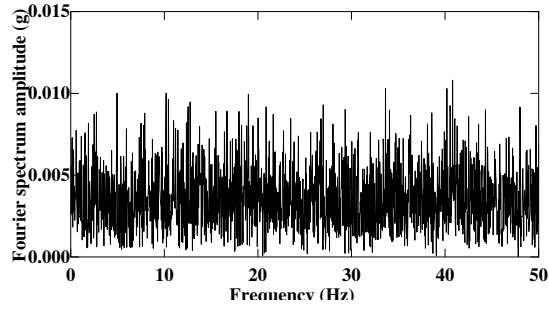
542

(a) 50° Slope



543

551



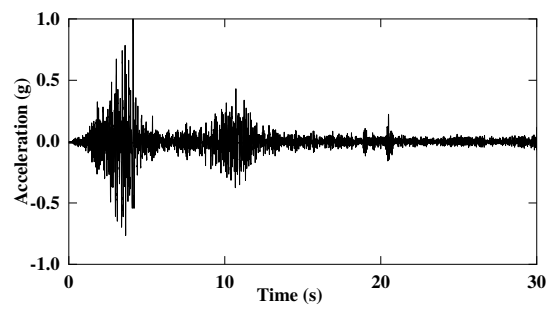
552

(b) Fourier spectrum

553

Fig.7 White noise wave

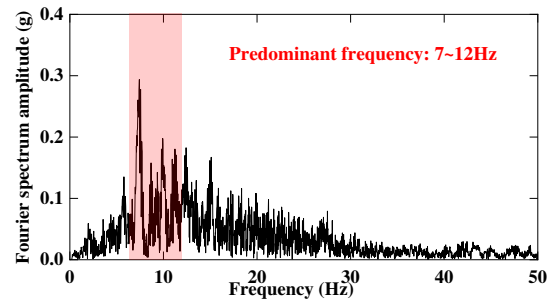
554



555

(a) Acceleration time history

556



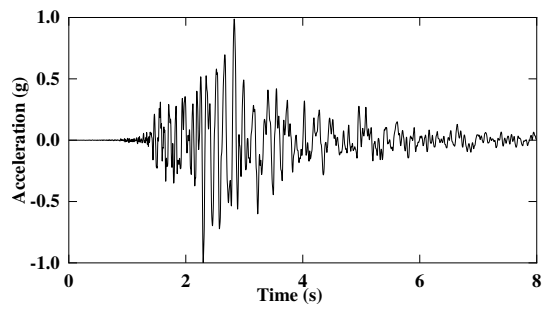
557

(b) Fourier spectrum

558

Fig.8 Wenchuan seismic wave

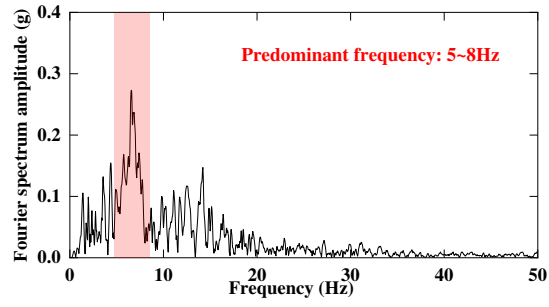
559



560

(a) Acceleration time history

561



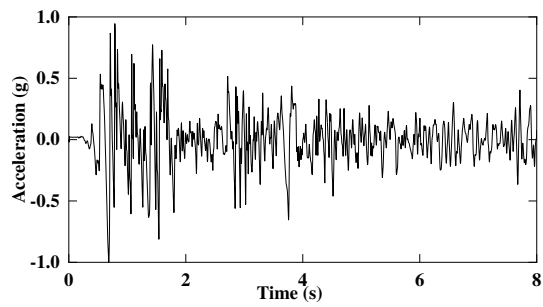
562

(b) Fourier spectrum

563

Fig.9 Kobe seismic wave

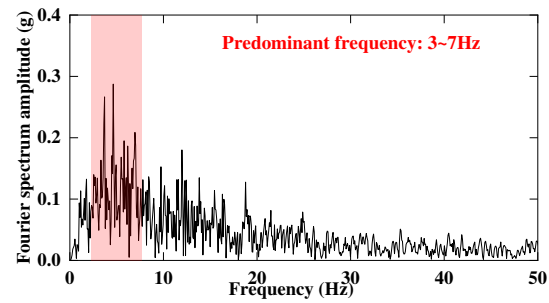
564



565

(a) Acceleration time history

566



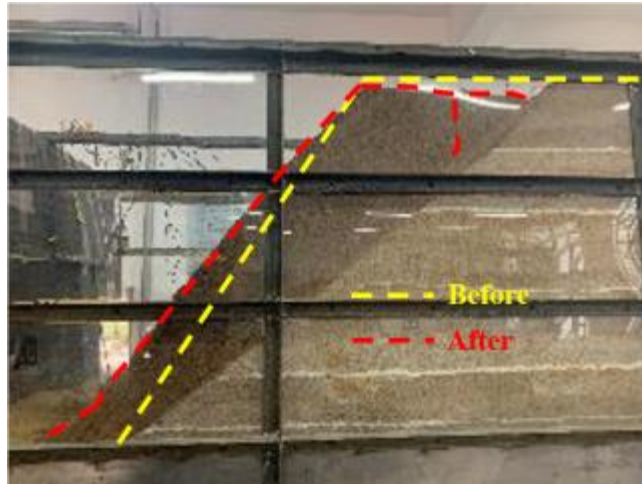
567

(b) Fourier spectrum

568

Fig.10 EL Centro seismic wave

569



570

(a) Slope deformation

571



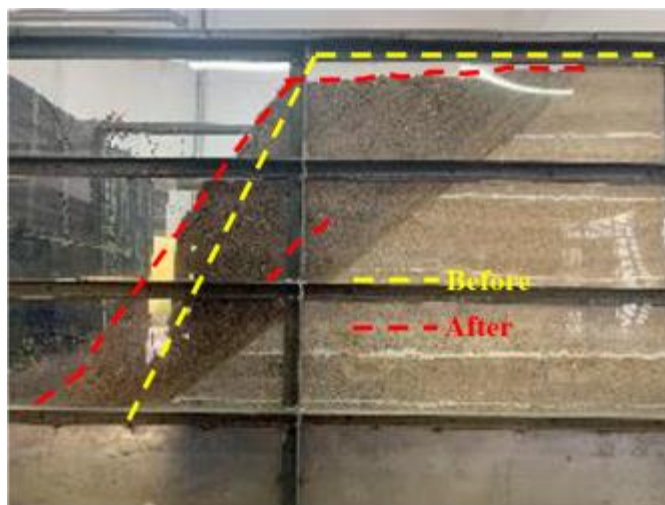
572

(b) Slope cracks and deformation

573

Fig.11 50° slope failure phenomenon

574



575

(a) Slope deformation



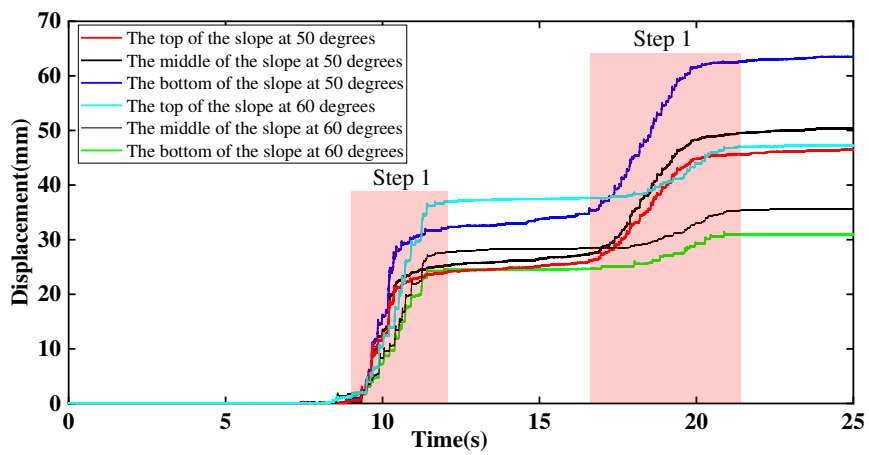
576

577

(b) Slope cracks and deformation

578

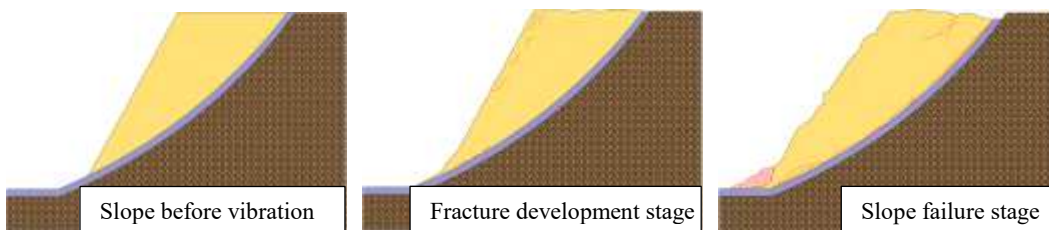
Fig.12 60° slope failure phenomenon



579

580

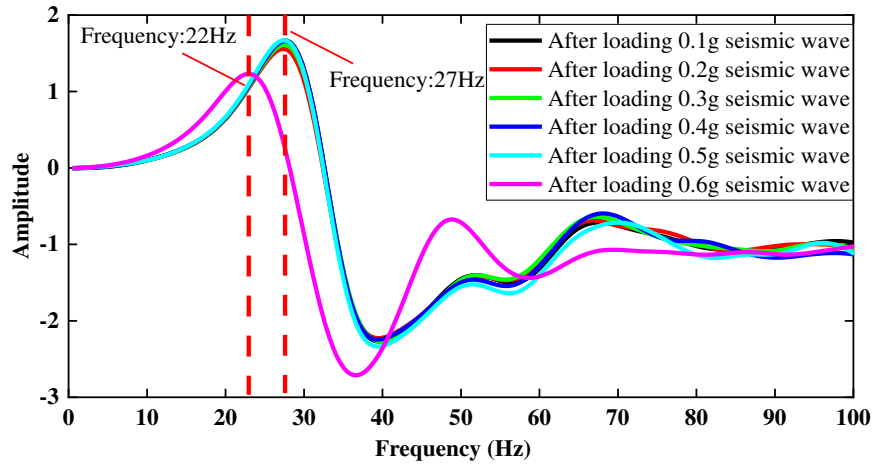
Fig.13 Slope surface displacement



581

582

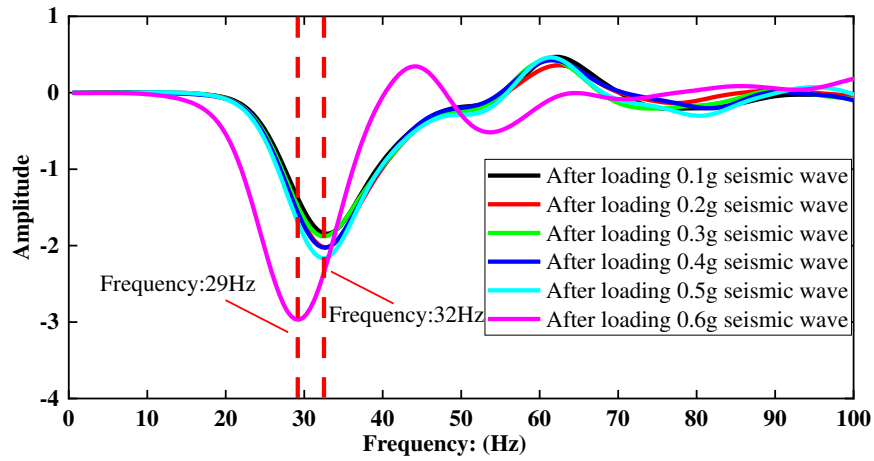
Fig.14 Diagrammatic drawing of slope collapse



583

584

(a) Real frequency



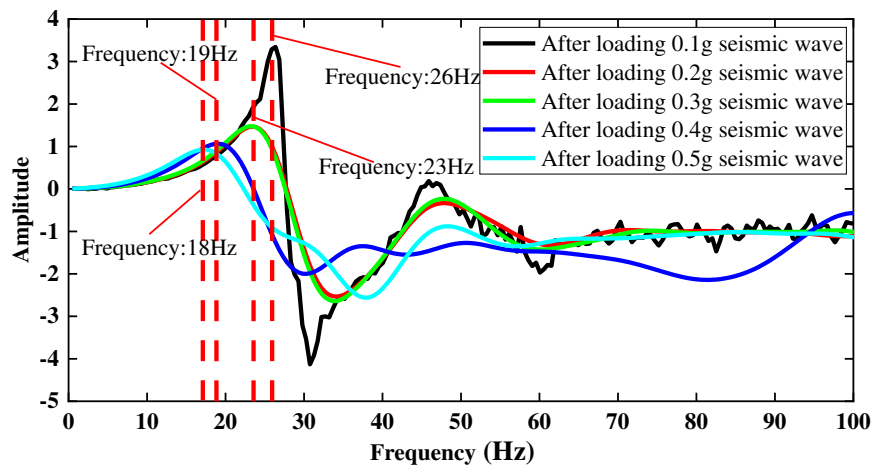
585

586

(b) Imaginary frequency

587

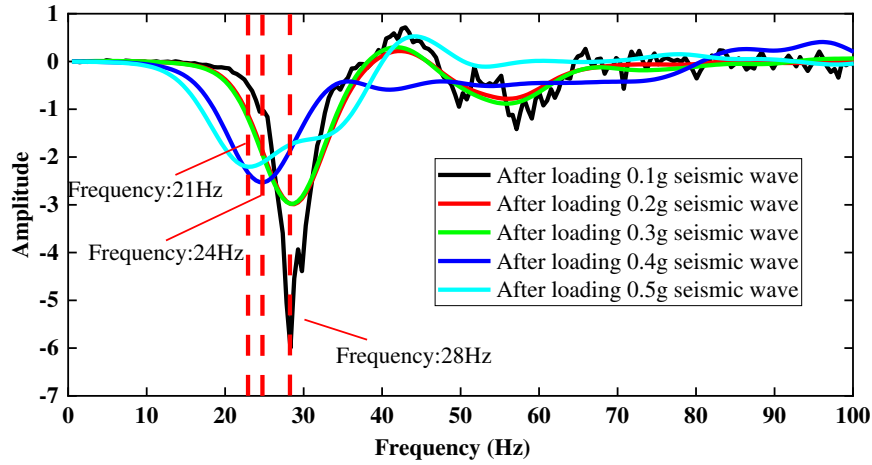
Fig.15 Frequency response function of measuring point A1 of 50° slope



588

589

(a) Real frequency



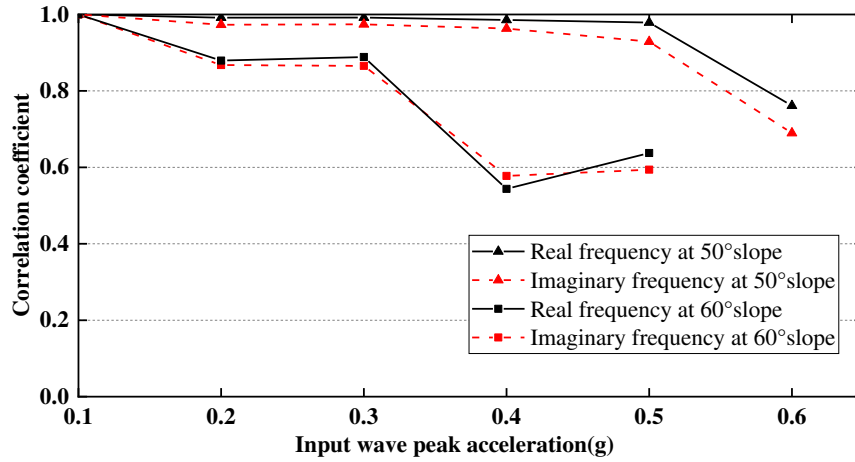
590

591

(b) Imaginary frequency

592

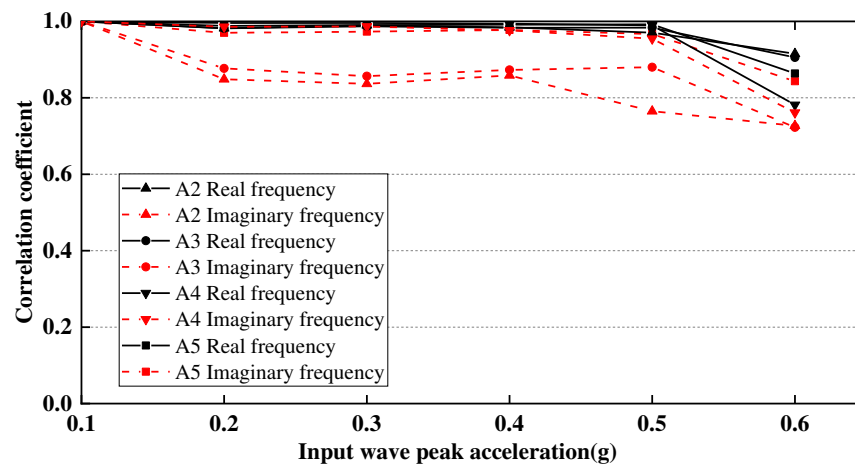
Fig.16 Frequency response function of measuring point A1 of 60° slope



593

594

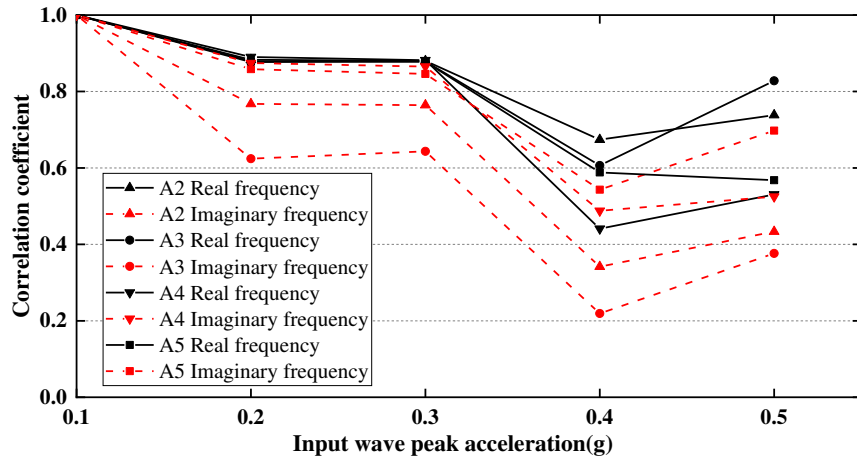
Fig.17 Frequency response function of measuring point A1 of 60° slope



595

596

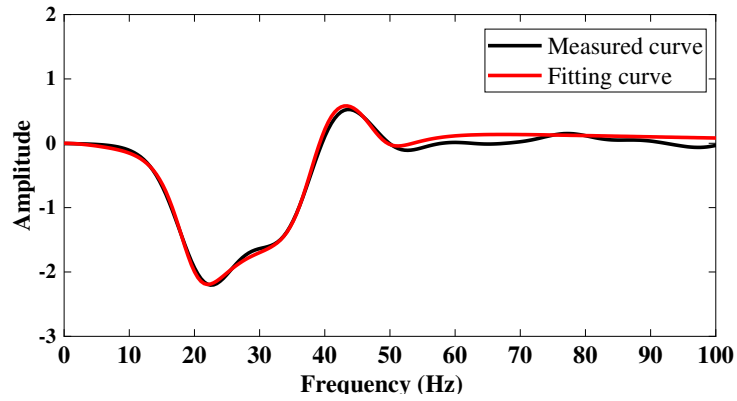
Fig.18 Frequency response function of measuring point A2-A5 of 50° slope



597

598

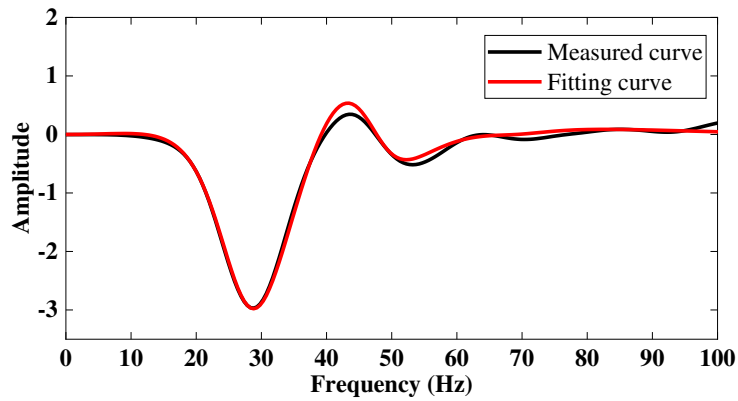
Fig.19 Frequency response function of measuring point A2-A5 of 60° slope



599

600

(a) 50° Slope after input of 0.6g peak acceleration seismic wave



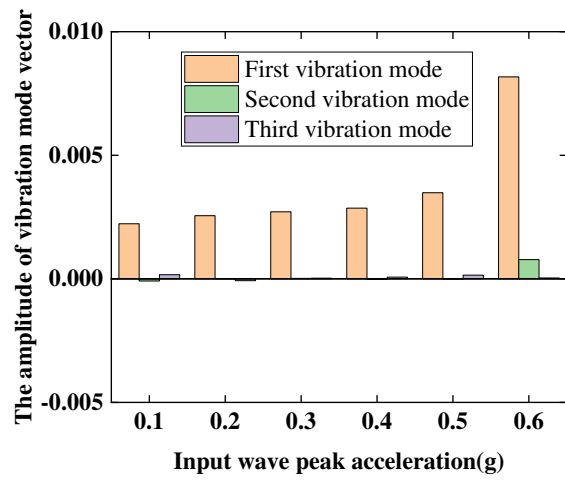
601

602

(b) 60° Slope after input of 0.5g peak acceleration seismic wave

603

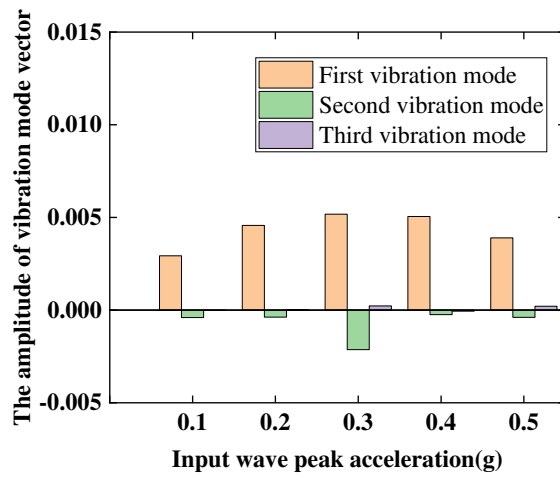
Fig.20 Imaginary frequency modal identification results of point A1s at slope failure



604

605

(a) 50° slope



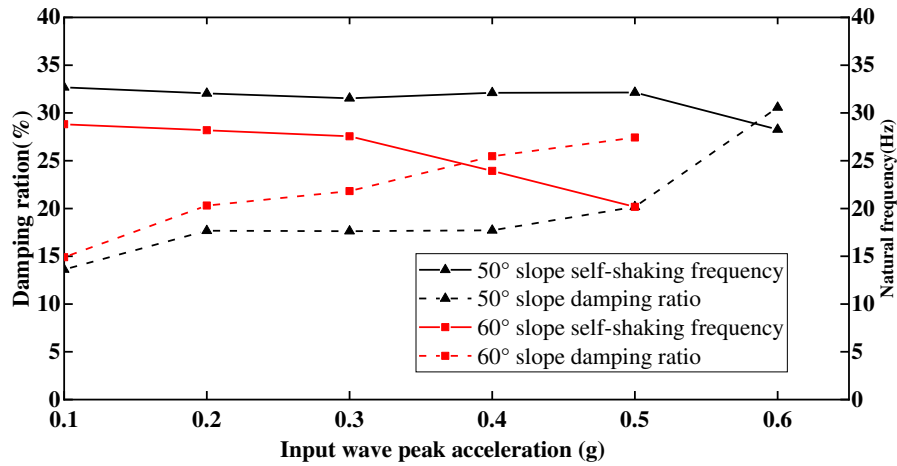
606

607

(b) 60° slope

608

Fig.21 The first three modes of vibration after the earthquake of the slope



609

610

Fig.22 Post-earthquake damping ratio and natural frequency of slope

611

Table 1 Similarity criterion derived by matrix method

| Physical quantity | c | φ | E | μ | v_s | g | A | T_d | s | θ | ε | σ | V | a | L | γ | ω | Relationship |
|-------------------|-------|-----------|-------|-------|-------|-------|-------|----------|----------|----------|---------------|----------|----------|----------|-------|----------|----------|---------------------------|
| | a_2 | a_3 | a_5 | a_6 | a_7 | a_8 | a_9 | a_{10} | a_{12} | a_{13} | a_{14} | a_{15} | a_{16} | a_{17} | a_1 | a_4 | a_{11} | |
| Target volume | | | | | | | | | | | | | | | | | | |
| π_1 | 1 | 0 | 0 | 0 | 0 | 0 | 0 | 0 | 0 | 0 | 0 | 0 | 0 | 0 | -1 | -1 | 0 | $\pi_1=c/L\gamma$ |
| π_2 | | 1 | 0 | 0 | 0 | 0 | 0 | 0 | 0 | 0 | 0 | 0 | 0 | 0 | 0 | 0 | 0 | $\pi_2=\varphi$ |
| π_3 | | | 1 | 0 | 0 | 0 | 0 | 0 | 0 | 0 | 0 | 0 | 0 | 0 | -1 | -1 | 0 | $\pi_3=E/L\gamma$ |
| π_4 | | | | 1 | 0 | 0 | 0 | 0 | 0 | 0 | 0 | 0 | 0 | 0 | 0 | 0 | 0 | $\pi_4=\mu$ |
| π_5 | | | | | 1 | 0 | 0 | 0 | 0 | 0 | 0 | 0 | 0 | 0 | -1 | 0 | -1 | $\pi_5=v_s/L\omega$ |
| π_6 | | | | | | 1 | 0 | 0 | 0 | 0 | 0 | 0 | 0 | 0 | -1 | 0 | -2 | $\pi_6=g/L\omega^2$ |
| π_7 | | | | | | | 1 | 0 | 0 | 0 | 0 | 0 | 0 | 0 | -1 | 0 | -2 | $\pi_7=A/L\omega^2$ |
| π_8 | | | | | | | | 1 | 0 | 0 | 0 | 0 | 0 | 0 | 0 | 0 | 1 | $\pi_8=T_d\omega$ |
| π_9 | | | | | | | | | 1 | 0 | 0 | 0 | 0 | 0 | -1 | 0 | 0 | $\pi_9=c/L\gamma$ |
| π_{10} | | | | | | | | | | 1 | 0 | 0 | 0 | 0 | 0 | 0 | 0 | $\pi_{10}=\theta$ |
| π_{11} | | | | | | | | | | | 1 | 0 | 0 | 0 | 0 | 0 | 0 | $\pi_{11}=\varepsilon$ |
| π_{12} | | | | | | | | | | | | 1 | 0 | 0 | -1 | -1 | 0 | $\pi_{12}=\sigma/L\gamma$ |
| π_{13} | | | | | | | | | | | | | 1 | 0 | -1 | 0 | -1 | $\pi_{13}=V/L\omega$ |
| π_{14} | | | | | | | | | | | | | | 1 | -1 | 0 | -2 | $\pi_{14}=a/L\omega^2$ |

612

Table 2 The similarity ratio of main physical quantities in the test model

| Physical quantities | Symbols and relation expression | Similitude parameter |
|-----------------------------------|---------------------------------|----------------------|
| Geometry L | C_L | 10 |
| Soil weight γ | C_γ | 1 |
| Duration T_d | $C_{T_d} = C_L^{0.5}$ | 3.16 |
| Cohesion C | $C_C = C_L$ | 10 |
| Internal friction angle φ | $C_\varphi = 1$ | 1 |
| Dynamic modulus of elasticity E | $C_E = C_L$ | 10 |

| | | |
|------------------------------------|------------------------|-------|
| Poisson ratio μ | $C_\mu = 1$ | 1 |
| Shear wave velocity V_s | $C_{V_s} = C_L^{0.5}$ | 3.16 |
| Gravity accelerometer g | $C_g = 1$ | 1 |
| Input vibration frequency ω | $C_\omega = C_L^{0.5}$ | 0.316 |
| Input acceleration A | $C_A = 1$ | 1 |
| Output acceleration a | $C_a = 1$ | 1 |

613

Table 3 Material parameters

| Structure type | Density (g/cm ³) | Cohesion (kPa) | Internal friction angle (°) |
|-------------------|------------------------------|----------------|-----------------------------|
| Accumulation mass | 1.908 | 1.55 | 37.9 |
| Weak interlayer | 1.72 | 0.27 | 41.7 |
| Bedrock | 2.206 | 43 | 38.91 |

614

Table 4 Loading cases included in the test

| 50°slope | | | | 60°slope | | | |
|--------------------|--------------------|--------------------------------|--------------------|--------------------------------|--------------------|--------------------------------|--------------------|
| Peak accelerations | Type of input wave | Excitations peak accelerations | Type of input wave | Excitations peak accelerations | Type of input wave | Excitations peak accelerations | Type of input wave |
| 0.05g | White noise | 0.05g | White noise | 0.05g | White noise | 0.05g | White noise |
| 0.1g | Earthquake wave | 0.4g | Earthquake wave | 0.1g | Earthquake wave | 0.4g | Earthquake wave |
| 0.05g | White noise | 0.05g | White noise | 0.05g | White noise | 0.05g | White noise |
| 0.2g | Earthquake wave | 0.5g | Earthquake wave | 0.2g | Earthquake wave | 0.5g | Earthquake wave |
| 0.05g | White noise | 0.05g | White noise | 0.05g | White noise | 0.05g | White noise |
| 0.3g | Earthquake wave | 0.6g | Earthquake wave | 0.3g | Earthquake wave | 0.3g | Earthquake wave |

615

Table 5 Criterion of correlation coefficient

| The correlation coefficient | The related degree |
|-----------------------------|-------------------------|
| 0.00-±0.30 | Micro correlation |
| ±0.30-±0.50 | Actual correlation |
| ±0.50-±0.80 | Significant correlation |
| ±0.80-±1.00 | Highly correlated |

616